Multi-Solvent Microdroplet Evaporation: Modeling and Measurement of Spray-Drying Kinetics with Inhalable Pharmaceutics

Mani Ordoubadi[1], Florence K. A. Gregson[2], Omar Melhem[1], David Barona[1], Rachael E. H. Miles[2], Dexter D'Sa[4], Sandra Gracin[3], David Lechuga-Ballesteros[4], Jonathan P. Reid[2], Warren H. Finlay[1], Reinhard Vehring[1,*]

[1]Department of Mechanical Engineering, University of Alberta, Edmonton, Alberta, Canada

[2]School of Chemistry, University of Bristol, Bristol, United Kingdom

[3]Pharmaceutical Technology & Development, AstraZeneca R&D Gothenburg, Sweden

[4]Pharmaceutical Technology & Development, AstraZeneca R&D South San Francisco, California, USA

Running Head: Kinetics of Spray-Drying Co-Solvent Solutions

*** Corresponding Author:**

Prof. Reinhard Vehring

University of Alberta, Department of Mechanical Engineering

10-203 Donadeo Innovation Centre for Engineering

9211 116 th Street NW, Edmonton, Alberta, T6G 1H9, Canada

Telephone: +1 780 492 5180

E-mail: reinhard.vehring@ualberta.ca

Abstract

Purpose Evaporation and particle formation from multi-solvent microdroplets containing solid excipients pertaining to spray-drying of therapeutic agents intended for lung delivery were studied. Various water and ethanol co-solvent systems containing a variety of actives and excipients (beclomethasone, budesonide, leucine, and trehalose) were considered.

Methods Numerical methods were used to predict the droplet evaporation rates and internal solute transfers, and their results verified and compared with results from two separate experimental setups. In particular, an electrodynamic balance was used to measure the evaporation rates of multicomponent droplets and a monodisperse droplet chain setup collected dried microparticles for further analytical investigations and ultramicroscopy.

Results The numerical results are used to explain the different particle morphologies dried from solutions at different co-solvent compositions. The obtained numerical data clearly show that the two parameters controlling the general morphology of a dried particle, namely the Péclet number and the degree of saturation, can change with time in a multi-solvent droplet. This fact complicates product development for such systems. However, this additional complexity vanishes at what we define as the iso-compositional point, which occurs when the solvent ratios and other composition-dependent properties of the droplet remain constant during evaporation, similar to the azeotrope of such systems during distillation.

Conclusions Numerical and experimental analysis of multi-solvent systems indicate that spray-drying near the iso-compositional ratio simplifies the design and process development of such systems.

Keywords Multi-solvent spray-drying, co-solvents, particle engineering, inhaled therapeutics, microparticles

Introduction

The study of evaporation and condensation of volatile components from microdroplets is important in many areas of engineering, pharmaceutics, medicine and environmental sciences (1–5). The studies pertaining specifically to inhalable therapeutics are of great significance, as these hygroscopic aerosols

can undergo severe morphological transformations due to mass and heat transfer in different environmental conditions ranging from the hot and relatively dry settings in spray-dryers (6) to the highly humid passages of the respiratory tract (7). In many of these circumstances, such as spray-drying from a co-solvent system (8,9) or the condensation of water on a propellant droplet (10), there is more than one volatile component inside the droplet. Models and analytical techniques can reduce the time, cost and risks associated with experimentation during the design and study of spray-dried particles (11,12). In spray-drying from single volatile components, the initial solute saturation and a dimensionless number called the Péclet number, which typically has a constant value for a single solvent droplet, determine the general morphology of the dried particles at different drying conditions (11). In an evaporating multi-solvent droplet, complications arise in the prediction and design stage as the composition of the droplet, its temperature, evaporation rate and the solubilities of the excipients change over the drying time, further highlighting the need for a numerical model in order to understand the underlying physics.

The study of evaporation of multicomponent droplets is specifically prevalent in fuel spray and combustion applications (5,13–16) and environmental aerosol and cloud formation (17). Assuming one-dimensional heat and mass transfers around and inside the droplet, the two models that have been used most frequently to model evaporation or condensation of a single aerosol droplet are the Maxwell model, which neglects the radial convective fluxes around the droplet, and the Stefan-Fuchs model, which accounts for these radial mass fluxes commonly known as Stefan flow (5,18). In this study, modified versions of these models appropriate for multi-solvent microdroplets are compared to assess their applicability in microparticle formation studies based on accuracy and levels of complexity.

There is a growing interest in using multi-solvent formulations in spray-drying hydrophobic active pharmaceutical ingredients such as budesonide (8), beclometasone dipropionate (19), triamcinolone acetonide (20) and fluticasone propionate (21) in order to achieve reasonable feed solute concentrations, production yield, dispersibility, and particle aerodynamic properties. Therefore, predictions of the evaporation and solvent compositions of co-solvent droplets containing such actives are useful during

their design and development stages. However, the different mechanisms of particle formation in such systems have yet to be studied comprehensively.

The evaporation rates and drying kinetics of microdroplets are usually studied experimentally via the use of single particle methods such as optical traps (22), electrodynamic balances (EDBs) (2,23) and droplet chain instruments (24–26).

In this study, verification of a numerical model is provided from measurements made with a Comparative-Kinetics Electrodynamic Balance (CK-EDB), which can levitate a single micron-sized aerosol droplet indefinitely. Light scattering can be used to infer the time-dependence of the droplet size with high accuracy in a controlled environment. Dry particle collection for comparison with the model predictions is performed using an in-house monodisperse droplet chain setup, which generates monodisperse particles. Even though imaging of the droplet chain facilitates the determination of droplet evaporation rates, this instrument is used here for the sole purpose of particle collection, as the CK-EDB outperforms it in sizing accuracy.

To assess the applicability of the numerical model in predicting the drying behavior and morphology of spray-dried microdroplets, the evaporation dynamics of various microdroplets containing different mixtures of water and ethanol are compared to our experimental data.

Materials and Methods

Materials

Trehalose dihydrate and L-leucine were purchased from Fisher Scientific (Ottawa, ON, Canada). The solvents used were absolute grade ethanol with purity of greater than 99.8% purchased from Sigma Aldrich (Oakville, ON, Canada) and HPLC grade water from Fisher Scientific (Ottawa, ON, Canada).

Comparative-Kinetics Electrodynamic Balance (CK-EDB)

The evaporation rates of multicomponent droplets were measured over a range of environmental conditions using a Comparative-Kinetics Electrodynamic Balance (CK-EDB) in which single aerosol droplets consisting of a mixture of water and ethanol were levitated. This technique has been described in detail in a previous publication (23) and is only briefly outlined here: A charged droplet with an initial diameter of approximately 44 μm of known composition was generated by a droplet-on-demand dispenser (MJ-ABP-01, MicroFab Technologies, Plano, Texas, USA) and injected into the center of the chamber of the instrument. The droplet was trapped within an electric field produced by two sets of concentric cylindrical electrodes, mounted vertically above one another. An AC voltage was applied to the electrodes, with an additional DC voltage superimposed across the bottom set of electrodes to counteract the gravitational force of the droplet. This technique allowed for stable trapping of charged droplets throughout the evaporation process. A gas flow formed from mixing wet and dry nitrogen gas streams passed over the droplet, permitting accurate control of relative humidity (RH) in the chamber ranging from 0 to about 95%. This stream flows with a velocity of about 3 cm/s inside the drying chamber during the measurements. Based on the available corrections (5), this flow with a Reynolds number of about 0.1 around a droplet with a diameter of 50 μm increases the Nusselt and Sherwood numbers of the evaporating droplet by less than 1% compared to a stationary droplet. Hence this gas velocity can be neglected in the calculations of the evaporation rates discussed in the theoretical section of this study. The RH is determined by comparing the evaporation kinetics of a probe droplet, of either NaCl solution or water, to a simulation using the Kulmala model (27). This method to determine the RH has an accuracy of approximately ±1% and is outlined in greater detail in a previous publication (2). In addition, the temperature of the CK-EDB chamber was controlled in a range from 0 °C to 25 °C by a recirculating ethylene glycol coolant. The error in the temperature determination using the thermocouple is ±0.5 °C. An overview of this instrument is shown in Figure 1(a).

A 532 nm CW laser illuminated the droplet, and the resulting scattering pattern caused by the interference between reflection and refraction at the droplet surface, i.e. the phase-function was collected at an angular range of ~ 24° by a CCD mounted at 45° to the direction of laser propagation. The angular separation between the fringes in the phase-function was used to calculate the radius of the droplet using a geometrical optics approximation, with an associated error of ±100 nm (2).

Monodisperse Droplet Chain Instrument

The monodisperse droplet chain setup used in this study was a modified version of an in-house instrument discussed in more detail previously (24,25). This instrument consisted of three main subsystems: feeding, imaging, and collection, as illustrated in Figure 1(b). The specific solution for each experiment was passed through two 0.45 μm pore sized syringe filters (SLHN033NS, EMD Millipore, Darmstadt, Germany) into an S-shaped reservoir with a volume of 3 mL. It was then dispensed using a high-temperature piezoceramic dispenser (MJ-AL-HT-40-8mx, MicroFab Technologies, Plano, Texas, USA), with an orifice diameter of 40 μm. The piezoceramic dispenser was operated by a driver (MD-E-3000 Microdrop Technologies, Norderstedt, Germany), which allowed control over the applied voltage and frequency. The voltage and frequency of the dispenser directly affect the initial diameter, production frequency of the droplets in the chain and the injection velocity. The solution droplets were injected into a heated airflow with a controlled flow rate in a circular flow tube, which had two walls to assist in temperature control. An imaging system with a high magnification lens (35-41-41-000, Excelitas, Fremont, California, USA), attached to a camera (GO-5000M-USB, JAI, Shanghai, China) was used to capture images of the droplet at the injection point which were later analyzed to determine the initial droplet diameter. Dried particles were collected for data analysis at the end of the flow tube using custom-made scanning electron microscope (SEM) sample stubs onto which a membrane filter (0.8 μm Isopore Polycarbonate, Millipore, Darmstadt, Germany) was attached using a double-sided adhesive carbon tape. Collected particles were coated with a vacuum gold sputter (Desk II, Denton Vacuum LLC, Moorestown,

NJ, USA) and analyzed using field emission scanning electron microscopy (Sigma FESEM, Zeiss, Jena, Germany) with an accelerating voltage of 5 kV and an average working distance of 6 mm. A number of sample particles were also imaged using helium-ion microscopy (ORION NanoFAB HIM with Ga FIB, Zeiss, Jena, Germany) at an accelerating voltage of 29 KV, an average working distance of 9 mm and using a 10 µm aperture; the particles were cut using a gallium-focused-ion beam (Ga-FIB) from the same instrument at an accelerating current of 300 pA with dwell times between 0.5 and 1.0 µs and beam spacing between 2 and 5 nm for fine and rough cuts, respectively.

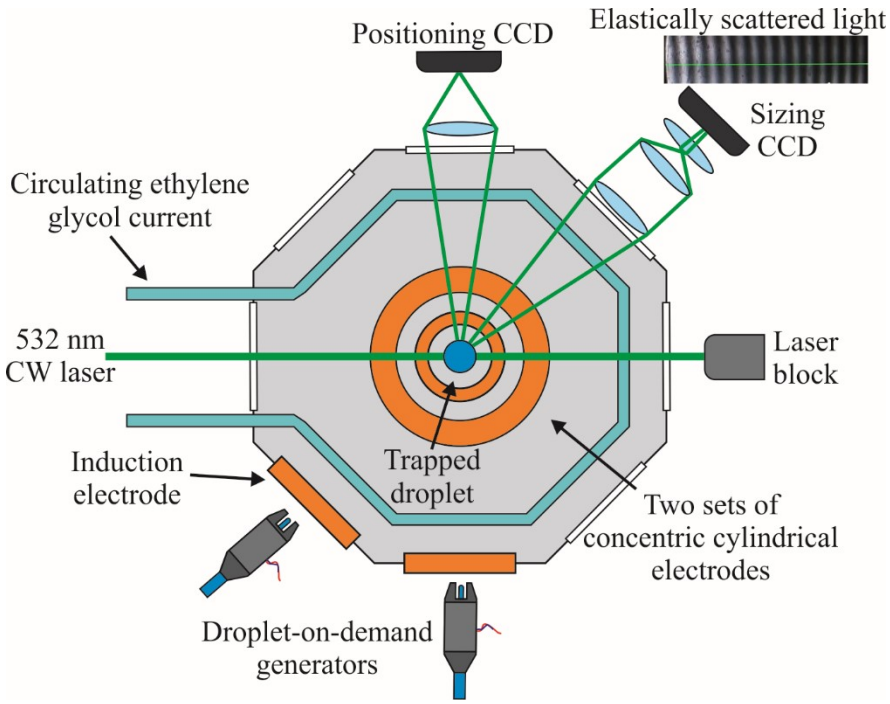

(a)

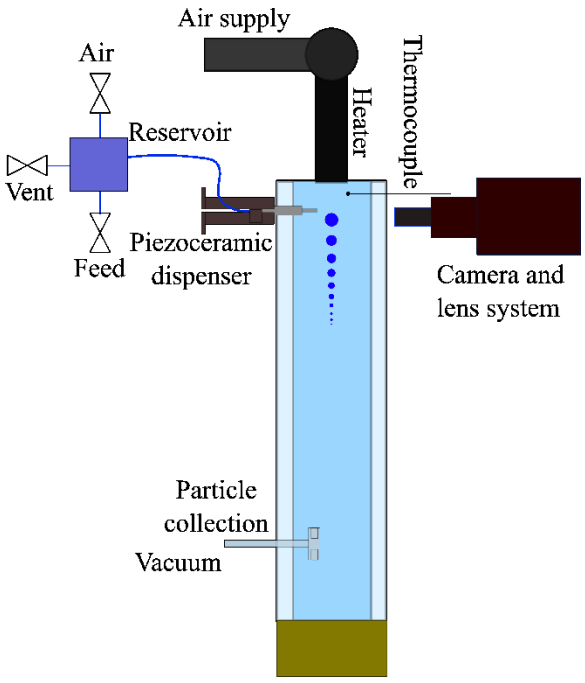

(b)

Figure 1 The experimental instruments, (a) CK-EDB, (b) Droplet chain setup.

Theory and Modeling of Multicomponent Evaporation and Particle Formation

Two different methods of increasing complexity were used to study the evaporation of multi-component microdroplets relevant to pharmaceutical applications. The first method is based on Maxwell's solution of mass transfer from a spherical liquid droplet in a quiescent environment (28,29). This quasi-steady model was modified for a multi-component droplet to account for the simultaneous evaporation or condensation of different volatile species (30). It does not, however, account for the interaction of different vapors in the gas phase and assumes no bulk radial velocity or Stefan flow around the droplet.

The second method is based on the analytical solution of mass and energy transport equations with the inclusion of radial convection in the gas phase. For a single component droplet, this methodology

produces the results of Fuchs (18) and is sometimes called the Stefan-Fuchs method (5). In both of these schemes, the mass transfer of each volatile component in the gas phase is considered independently of the transfer of other species and the diffusion obeys Fick's law (29,31). Inclusion of inter-species diffusion effects during the evaporation or condensation of multicomponent droplets requires a full Maxwell–Stefan diffusion model (15) and is beyond the scope of this study; it will be seen later that the simplified models have the required accuracy pertaining to spray-drying of pharmaceutical particles.

In both models, some assumptions and simplifications were made based on the specific conditions prevailing in pharmaceutical processes. Some of these conditions include small droplets (diameter: 5-50 μm), low settling velocity and Reynolds numbers, and low-to-moderate temperatures (less than 150 °C gas temperature). The assumptions are as follows:

1. Spherical symmetry and negligible droplet motion with respect to the gas phase
2. Quasi-steadiness in the gas phase
3. Negligible Soret and Dufour effects and radiation heat transfer
4. Negligible Kelvin effect
5. Continuum regime
6. Infinite thermal and solvent mass diffusivity in the droplet (well-mixed approximation)

The spherical symmetry assumption is justified because of the small size of the droplets encountered in spray-drying of pharmaceutics or emitted from different inhalers. At diameters of less than 50 μm, the settling velocities and relaxation times are small enough to neglect internal convection (28). The Knudsen number is also small enough at atmospheric conditions to neglect non-continuum corrections. As an example, for an ethanol droplet with a diameter of 50 μm evaporating in air with a temperature of 80 °C, the settling velocity and relaxation time are about 60 mm/s and 6 ms, respectively. The droplets might have larger initial velocities upon atomization but will reach their terminal or settling velocity in a time comparable to the relaxation time. The time it takes for complete evaporation for a droplet of this size at this temperature is about 0.15 s, which is about 25 times the relaxation time. Thus, the initial transient

phase is a small fraction of the total droplet lifetime, and the effects of the internal circulation in this phase can be neglected given the longer life span of the droplet. At the terminal velocity, the droplet has a Reynolds number of about 0.14, so that neglecting the relative droplet motion with respect to the gas phase will under-predict the Nusselt and Sherwood numbers by only about 2% (5,32). Assuming quasi-steady evaporation requires that any changes in the boundary conditions at the droplet-gas interface instantaneously appear in the gas conditions around the droplet. In other words, transient effects are neglected in the solution of the mass and energy transports in the gas phase (18,28,33). The characteristic time required for the thermal and composition profiles around a droplet to reach equilibrium, t_t, can be approximated as (33,34):

$$t_t = \frac{d^2}{16\alpha_v} \tag{1}$$

where d is the droplet diameter and α_v is the appropriate diffusivity in the gas phase, i.e. either the thermal diffusivity or the mass diffusion coefficient of the vapor. For a 50 μm diameter ethanol droplet in air, the time scales associated with thermal and mass diffusion are approximately equal to 7 and 14 μs, respectively, which are small enough compared to the droplet lifetime to justify the quasi-steady assumption.

Similarly, the well-mixed assumption for the interior of the droplet is based on the low temperature and small diameter ranges encountered in the applications pertaining to this study. At these conditions, the solvent diffusion and thermal conduction is fast enough to assume constant radial profiles for the solvent compositions and temperatures inside the droplet (35).

In both models, numerical integration is performed using a simple first-order Euler method to advance in time. During each time-step, the droplet composition and temperature are updated based on the analytical solutions of the mass and energy transport in the gas phase.

Maxwell Model

In the absence of any bulk radial gas flow, the solution of Fick's law of diffusion with the appropriate boundary conditions provides the mass transfer rate, $\dot{m}$, of a single-solvent droplet as (28):

$$\dot{m} = -2\pi d D (C_{\mathrm{s}} - C_{\infty}) \tag{2}$$

in which d is the droplet diameter and D is the binary diffusion coefficient of the vapor in the gas. C_{s} and C_{∞} are the vapor mass concentrations near the droplet surface and at infinity, respectively.

If it can be assumed that the diffusion of each volatile component in the gas phase is independent of the others, different mass transfer rates of separate species of a multicomponent droplet can be superimposed in accordance with Equation 2. Hence, the total mass transfer rate from the droplet, $\dot{m}_{\mathrm{t}}$, can be obtained from the following equation:

$$\dot{m}_{\mathrm{t}} = \sum \dot{m}_i = \sum_i -2\pi d D_{\mathrm{v},i} \left(C_{\mathrm{s},i} - C_{\infty,i}\right) \tag{3}$$

in which $D_{\mathrm{v},i}$ is the diffusion coefficient of the *i*th volatile component in the gas mixture at an intermediate temperature and gas composition, which will be discussed later (*cf*. Equations 11 and 12). By assuming equilibrium between the vapor and the liquid phases at the interface, the surface vapor concentration, $C_{\mathrm{s},i}$, can be obtained from the modified Raoult's law as:

$$C_{\mathrm{s},i} = x_{\mathrm{ls},i} \frac{P_{\mathrm{sat},i}(T_{\mathrm{d}}) M_i}{R T_{\mathrm{d}}} \gamma_i \tag{4}$$

where $x_{\mathrm{ls},i}$ is the molar fraction of the *i*th component in the liquid at the surface, and $P_{\mathrm{sat},i}(T_{\mathrm{d}})$ is the saturation vapor pressure, which can be obtained from Clausius–Clapeyron or Antoine equations at the droplet temperature, T_{d}. M_i and γ_i are the molar mass and activity coefficient of the *i*th component, respectively, and R is the universal gas constant. In this study, the activity coefficients are calculated

using the NRTL method (36). The vapor concentration far away from the droplet can be obtained from the partial pressure of each component, $P_{\infty,i}$, as:

$$C_{\infty,i} = \frac{P_{\infty,i} M_i}{R T_\infty} \tag{5}$$

To find the droplet temperature according to the infinite thermal conductivity or lumped-capacitance assumption inside the droplet, the following relationship is used (28):

$$\rho_{\mathrm{l}} c_{\mathrm{p,l}} \frac{d^2}{12} \frac{\mathrm{d}T_{\mathrm{d}}}{\mathrm{d}t} = -\bar{k}(T_{\mathrm{d}} - T_\infty) - \sum L_i D_{\mathrm{v},i} \left(C_{\mathrm{s,i}} - C_{\infty,i}\right) \tag{6}$$

where ρ_{l} is the liquid mixture density, $c_{\mathrm{p,l}}$ is the specific heat of the liquid mixture, $\bar{k}$ is the gas thermal conductivity at the intermediate conditions and L_i is the latent heat of vaporization of each material.

At each time-step, Equations 3 and 6 are solved and the composition and temperature of the droplet are updated. In order to obtain the droplet size, the following mass balance is used:

$$\frac{\pi}{6} \frac{\mathrm{d}(\rho_{\mathrm{l}} d^3)}{\mathrm{d}t} = \dot{m}_{\mathrm{t}} \tag{7}$$

Noting that the composition and the temperature of the droplet are changing temporally, Equation 7 can be rewritten as:

$$\frac{\mathrm{d}d}{\mathrm{d}t} = \frac{2\dot{m}_{\mathrm{t}}}{\pi \rho_{\mathrm{l}} d^2} - \frac{d}{3\rho_{\mathrm{l}}} \frac{\mathrm{d}\rho_{\mathrm{l}}}{\mathrm{d}t} \tag{8}$$

By knowing the new and previous droplet compositions and temperatures, the time derivative of the droplet density can be approximated using first order discretization, and the new droplet diameter is

obtained at the end of each time-step. Using Equation 8, the thermal and compositional expansion and shrinkage of the droplet can be accurately modeled if an accurate correlation for the mixture density is used. For instance, for water/ethanol mixtures, the following semi-empirical relationship is used (37):

$$\ln \rho_{\mathrm{l}} = x_{\mathrm{l,w}} \ln \rho_{\mathrm{l,w}} + x_{\mathrm{l,eth}} \ln \rho_{\mathrm{l,eth}} - 30.808 \left(\frac{x_{\mathrm{l,w}} x_{\mathrm{l,eth}}}{T_{\mathrm{d}}} \right) - 18.274 \left[\frac{x_{\mathrm{l,w}} x_{\mathrm{l,eth}} \left(x_{\mathrm{l,w}} - x_{\mathrm{l,eth}} \right)}{T_{\mathrm{d}}} \right] + 13.89 \left[\frac{x_{\mathrm{l,w}} x_{\mathrm{l,eth}} \left(x_{\mathrm{l,w}} - x_{\mathrm{l,eth}} \right)^2}{T_{\mathrm{d}}} \right] \tag{9}$$

where $x_{\mathrm{l,w}}$ and $x_{\mathrm{l,eth}}$ are the mole fractions of water and ethanol in the droplet, respectively; $\rho_{\mathrm{l,w}}$ and $\rho_{\mathrm{l,eth}}$ are their respective temperature-dependent liquid densities in kg/m^3 and T_{d} is the droplet temperature in K. In the absence of such empirical relations for the mixture of interest, one can use the following relationship for the mixture density assuming ideal mixing:

$$\frac{1}{\rho_{\mathrm{l}}} = \sum \frac{y_{\mathrm{l},i}}{\rho_{\mathrm{l},i}} \tag{10}$$

where, $y_{\mathrm{l},i}$ and $\rho_{\mathrm{l},i}$ are the mass fraction and liquid densities of the *i*th component in the droplet, respectively.

As mentioned previously, the transport properties in the gas phase of the droplet-gas interface are assumed to be radially constant. In this study, a 1/3 approximation has been used (5,26), according to which the intermediate temperature, $\bar{T}$, and intermediate mass fraction of the *i*th component in the gas phase, $\bar{y}_{\mathrm{g},i}$, are:

$$\bar{T} = \frac{2}{3} T_{\mathrm{d}} + \frac{1}{3} T_{\infty} \tag{11}$$

$$\bar{y}_{\mathrm{g},i} = \frac{2}{3} y_{\mathrm{s,g},i} + \frac{1}{3} y_{\infty,\mathrm{g},i} \tag{12}$$

where $y_{\mathrm{s,g},i}$ and $y_{\infty,\mathrm{g},i}$ are the mass fractions of the *i*th volatile component in the gas phase, near the surface and far from the surface of the droplet, respectively. This approximation becomes defective at very high drying gas temperatures, as observed in spray combustion applications; but it is sufficiently accurate for the mild temperatures encountered in pharmaceutical processes. These intermediate conditions are updated at the start of each time-step based on the droplet temperature of the last step.

Stefan-Fuchs Model

In the second model, the effects of the radial convection or Stefan Flow are considered. The governing transport equations in the gas phase are the mass transfer equations of the inert gas (e.g. air) and each of the volatile components as well as the energy transfer equation (16,29,31).

The quasi-steady equations governing the species transfer around the droplet for the inert gas and each component *i* are as follows:

$$\frac{\mathrm{d}}{\mathrm{d}r}\{4\pi r^2 n_{\mathrm{inert}}\} = \frac{\mathrm{d}}{\mathrm{d}r}\left\{4\pi r^2\left(C_{\mathrm{inert}}U - D_{\mathrm{inert,m}}\cdot\rho_{\mathrm{t}}\frac{\mathrm{d}y_{\mathrm{inert}}}{\mathrm{d}r}\right)\right\} = 0 \tag{13}$$

$$\frac{\mathrm{d}}{\mathrm{d}r}\{4\pi r^2 n_i\} = \frac{\mathrm{d}}{\mathrm{d}r}\left\{4\pi r^2\left(C_i U - D_{i,\mathrm{m}}\cdot\rho_{\mathrm{t}}\frac{\mathrm{d}y_{\mathrm{g},i}}{\mathrm{d}r}\right)\right\} = 0 \tag{14}$$

where n_{inert}, C_{inert}, $D_{\mathrm{inert,m}}$ and y_{inert} are the mass flux, mass concentration, diffusion coefficient in the mixture at the intermediate conditions and mass fraction of the inert gas, respectively. Similarly, n_i, $C_{\mathrm{g},i}$, $D_{i,\mathrm{m}}$ and $y_{\mathrm{g},i}$ are the mass flux (i.e. transferred mass per time and cross sectional area), mass concentration, diffusion coefficient in the gas mixture at the intermediate conditions (obtained from Equations 11 and 12) and mass fraction of each volatile component *i*. U and ρ_{t} are the bulk radial velocity of the gas and total gas density, respectively, and *r* is the radial coordinate. The summation of Equations

13 and 14 results in a relationship for the radial velocity, U, assuming that the inert gas mass flux, n_{inert}, is zero everywhere (due to the negligible solubility of air in the droplet). To write an explicit expression for the total evaporation rate from the droplet as a function of the radial velocity, it is usual to assume that the diffusion coefficients of all the components, including air, are equal. Note that the correct diffusion coefficient of each volatile component is maintained during the derivation of individual evaporation rates (31). The radial velocity is then given by:

$$U = -\frac{\dot{m}_{\mathrm{t}}}{4\pi r^2 \rho_{\mathrm{t}}} \tag{15}$$

Note that this equation is an approximation that is valid when the droplet density is much higher than the gas phase density, which is a reasonable assumption in this study. Combining Equations 13 and 15 and noting again that the mass flux of the inert gas (i.e. air) is zero results in an ordinary differential equation for the mass fraction of the inert gas whose solution, using the appropriate boundary conditions gives (29,31):

$$\dot{m}_{\mathrm{t}} = -2\pi d \rho_{\mathrm{t}} D_{\mathrm{inert,m}} \ln\left(\frac{y_{\infty,\mathrm{inert}}}{y_{\mathrm{s,inert}}}\right) \tag{16}$$

where $y_{\infty,\mathrm{inert}}$ and $y_{\mathrm{s,inert}}$ are the inert gas mass fractions far away from the droplet and near the surface, respectively. This relationship is the same as the one obtained by Fuchs for a single component droplet (18). The next step is to find the contribution of each individual volatile component to the droplet mass transfer by combining Equations 14 and 15 to result in a second order differential equation for the mass fractions of each of these components, the solution of which gives a relationship for $y_i(r)$ (31). To find $\dot{m}_i$, note that:

$$\dot{m}_i = -\pi d^2 n_i\big|_{r=\frac{d}{2}} = -\pi d^2 \left(C_i U\big|_{r=\frac{d}{2}} - \rho_{\mathrm{t}} D_{i,\mathrm{m}} \frac{\mathrm{d}y_i}{\mathrm{d}r}\bigg|_{r=\frac{d}{2}}\right) \tag{17}$$

Combining this with Equation 15 and the relationship obtained for $y_i(r)$, gives

$$\dot{m}_i = -2\pi d\rho_{\mathrm{t}} D_{\mathrm{inert,m}} \ln\left(\frac{y_{\infty,\mathrm{inert}}}{y_{\mathrm{s,inert}}}\right)\frac{y_{\infty,i}\beta_i - y_{\mathrm{s},i}}{\beta_i - 1} = \dot{m}_{\mathrm{t}}\frac{y_{\infty,i}\beta_i - y_{\mathrm{s},i}}{\beta_i - 1} \tag{18}$$

where $y_{\infty,i}$ and $y_{\mathrm{s},i}$ are the vapor mass fractions of the *i*th component far away from the droplet and near the surface, respectively, and

$$\beta_i = \left(\frac{y_{\mathrm{s,inert}}}{y_{\infty,\mathrm{inert}}}\right)^{\frac{D_{\mathrm{inert,m}}}{D_{i,\mathrm{m}}}}$$

A careful examination of Equation 18 reveals several important points. First, if there is only one solvent, then $\frac{D_{\mathrm{inert,m}}}{D_{i,\mathrm{m}}} = 1$ and this in turn will result in $\frac{\dot{m}_i}{\dot{m}_{\mathrm{t}}} = 1$ as expected. Second, if $\dot{m}_{\mathrm{t}} \to 0$ or $\frac{y_{\infty,\mathrm{inert}}}{y_{\mathrm{s,inert}}} \to 1$, then $\ln(\frac{y_{\infty,\mathrm{inert}}}{y_{\mathrm{s,inert}}}) \approx \frac{y_{\infty,\mathrm{inert}}}{y_{\mathrm{s,inert}}} - 1$ and $\beta_{\mathrm{i}} \approx 1 + \frac{D_{\mathrm{inert,m}}}{D_{i,\mathrm{m}}}\left(\frac{y_{\mathrm{s,inert}}}{y_{\infty,\mathrm{inert}}} - 1\right)$. If we define $\eta = \frac{y_{\mathrm{s,inert}}}{y_{\infty,\mathrm{inert}}}$, then:

$$\lim_{\eta\to 1}\dot{m}_i = -2\pi d\rho_{\mathrm{t}} D_{\mathrm{inert,m}} \lim_{\eta\to 1}\left\{\left(\frac{1}{\eta} - 1\right)\frac{y_{\infty,i}\left[1 + \frac{D_{\mathrm{inert,m}}}{D_{i,\mathrm{m}}}(\eta - 1)\right] - y_{\mathrm{s},i}}{1 + \frac{D_{\mathrm{inert,m}}}{D_{i,\mathrm{m}}}(\eta - 1) - 1}\right\}$$

Noting $\lim_{\eta\to 1}\frac{\frac{1}{\eta}-1}{\eta-1} = \lim_{\eta\to 1}\frac{\frac{1-\eta}{\eta}}{\eta-1} = -1$, the following is obtained in the limiting case when $\dot{m}_{\mathrm{t}}$ is approximately equal to zero:

$$\dot{m}_{\mathrm{i}} = -2\pi d\rho_{\mathrm{t}} D_{\mathrm{inert,m}}\left(y_{\mathrm{s},i} - y_{\infty,i}\right).$$

In this limiting case, the radial convection or Stefan flow, vanishes which is evident from Equation 15, and this equation is the same as Equation 3 based on Maxwell's solution. Note that individual components might have non-zero contributions to the droplet evaporation or condensation, but the total evaporation rate of the droplet can be zero when these contributions cancel out.

Lastly, as also noted in (31), there is a problem of inconsistency with Equation 18 since $\sum \dot{m}_i$ is not equal to $\dot{m}_\mathrm{t}$ from Equation 16. This is due to the previous assumption of equal mass diffusivities for different species in deriving Equation 16. The error due to this inconsistency is relatively small in most practical applications, as the vapor diffusivities of most species of interest are comparable.

The energy equation for the gas phase also contains the radial convective term shown in the following differential equation:

$$\frac{\mathrm{d}^2T}{\mathrm{d}r^2} + \left(\frac{2}{r} + \alpha_\mathrm{t}\frac{1}{r^2}\right)\frac{\mathrm{d}T}{\mathrm{d}r} = 0 \tag{19}$$

where

$$\alpha_\mathrm{t} = \frac{\sum \dot{m}_\mathrm{i} c_{\mathrm{p,g},i}}{4\pi k_\mathrm{film}}$$

Here $c_{\mathrm{p,g},i}$ is the specific heat of each vapor species. The solution of this equation with the boundary conditions at infinity, T_∞, and near the droplet surface, T_d, gives:

$$T = \frac{1}{\mathrm{e}^{\frac{2\alpha_\mathrm{t}}{d}} - 1}\left[\left(T_\infty \mathrm{e}^{\frac{2\alpha_\mathrm{t}}{d}} - T_\mathrm{d}\right) - (T_\infty - T_\mathrm{d})\mathrm{e}^{\frac{\alpha_\mathrm{t}}{r}}\right]. \tag{20}$$

The heat transfer to the droplet can be obtained from Equation 20 and used in the equation of energy balance for the droplet to give:

$$\frac{\mathrm{d}T_\mathrm{d}}{\mathrm{d}t} = \frac{6}{\rho_\mathrm{l} c_{\mathrm{p,l}} \pi d^3}\left[\frac{4\pi k_\mathrm{film}\alpha_\mathrm{t}}{e^{-\frac{2\alpha_\mathrm{t}}{d}} - 1}(T_\mathrm{d} - T_\infty) + \sum L_i \dot{m}_\mathrm{i}\right]. \tag{21}$$

Internal Solute Diffusion

The internal distribution of different solutes plays an important role in determining the dried particle morphology (11,26). As the droplets shrink during drying, there is a tendency for the solutes to enrich the surface. The established concentration gradient will cause the solutes to diffuse to the center of the droplet, in accordance with Fick's law of diffusion. Hence, the amount of surface enrichment is a consequence of two competing effects, the evaporation rate, κ, and the diffusion rate of each specific solute. The evaporation rate is defined as:

$$\kappa = -\frac{\mathrm{d}d^2}{\mathrm{d}t} \tag{22}$$

A careful scale analysis of Fick's second law of diffusion in an evaporating droplet shows that the competition of these mechanisms can be characterised by the Péclet number, Pe_j, defined as (26,38):

$$Pe_j = \frac{\kappa}{8D_j} \tag{23}$$

in which D_j is the diffusion coefficient of the jth solute in the droplet. A very large Péclet number, much larger than one, is consistent with a surface recession that is much faster than diffusion. This fact results in much larger surface concentrations of the solute than the average concentration inside the droplet, while the concentrations at other radial positions away from the surface are relatively constant and smaller. At the other extreme, with Péclet numbers of about one or less, the concentration is relatively uniform throughout the droplet. Péclet numbers between these two extremes will result in smooth concentration profiles with a minimum at the center and a maximum at the surface during evaporation. Note that these discussions are only valid under spherical symmetry inside and around the droplet and in the absence of internal convective transport.

For a solution droplet with only one solvent, both the evaporation rate and the diffusion coefficients of different species can often be assumed constant during the evaporation process, resulting in a constant Péclet number for each solute. This assumption is good as long as the dependence of the diffusion

coefficient on the solute concentration can be neglected, i.e. at moderate to low concentrations (39). For this case, an analytical model, known as the VFL model (11), has been previously developed to calculate the steady-state surface enrichment of each solute from the Péclet number. Surface enrichment, E_j, is defined as the instantaneous surface concentration of each solute, $C_j(\frac{d}{2}, t)$, divided by the instantaneous mean concentration of that solute, $C_{\mathrm{m},j}(t)$. These concentrations should not be confused with the vapor concentrations from the previous sections. In general, for a constant Péclet number, the surface enrichment undergoes a transient stage before converging to a constant value. The VFL model gives this steady-state surface enrichment value as (26):

$$E_{j,\mathrm{steady}} = \frac{C_j\left(\frac{d}{2}, t\right)}{C_{\mathrm{m},j}(t)} = 1 + \frac{Pe_j}{5} + \frac{Pe_j^2}{100} - \frac{Pe_j^3}{4000} \tag{24}$$

which is applicable for $Pe_j < 20$. The unsteady Fickian diffusion of solutes inside a single solvent droplet with a constant evaporation rate was solved in another study to account for the initial transient stages of the surface enrichment, and different correlations for different Péclet number regimes were presented (11). It was concluded that the initial transient stage is very short compared to the total droplet lifetime at small Péclet numbers, less than ~0.5. At larger Péclet numbers, the surface enrichment converges to the steady value only near the end of the droplet lifetime.

In the case of solutions with more than one volatile solvent, both the evaporation rate and the diffusion coefficients will generally change with time, resulting in a time-varying Péclet number. This fact requires the numerical solution of the internal diffusion of each solute at each time-step to obtain the concentration profiles. The one-dimensional Fick's law of diffusion inside an evaporating droplet in the spherical coordinate system is (11):

$$\frac{\partial C_j}{\partial t} = \frac{4D_j}{d^2}\left(\frac{\partial^2 C_j}{\partial R^2} + \frac{2}{R}\frac{\partial C_j}{\partial R}\right) - \frac{\kappa R}{2d^2}\frac{\partial C_j}{\partial R}, \tag{25}$$

where $R = \frac{r}{\frac{d(t)}{2}}$ is the non-dimensional radial coordinate, d is the instantaneous diameter of the droplet and κ, the evaporation rate is obtained from one of the two different methodologies discussed in the previous subsections. The appropriate initial and boundary conditions of this second order partial differential equation are:

$$\begin{cases} C_j = C_{0,j} & t = 0 \\ \dfrac{\partial C_j}{\partial R} = 0 & R = 0 \\ D_j \dfrac{\partial C_j}{\partial R} - \dfrac{\kappa}{8} C_j = 0 & R = 1 \end{cases}$$

D_j is assumed to be constant in the radial direction in arriving at Equation 25. In the case of a single solvent, D_j can be approximated as the diffusion coefficient at infinite dilution of each specific solute in the solvent as the effects of increasing concentration on the diffusion coefficients are neglected in the current study. The diffusion inside a droplet composed of more than one solvent is more complicated, and in general the use of a binary diffusion equation such as Equation 25 is not accurate. One could solve the Maxwell-Stefan or generalized Fick's equations to account for the interspecies diffusion (40). However, the solution of these equations requires knowledge of every binary diffusion coefficient of every component, either solvent or solute, in the other components to make up the diffusion coefficient matrix, which makes the use of such diffusion equations impractical in most cases. Instead, it is assumed that each solute behaves as if it were at infinite dilution in a single solvent, with the diffusion coefficient equal to a value dependent on the binary diffusion coefficients of this specific solute in each of the solvents as well as on the composition of the solvents. This simplification gives an exact relationship for dilute ideal gas mixtures based on Maxwell-Stefan theory (41,42) but introduces an error for dense gases and non-ideal liquids (40). For the water and ethanol binary system, the following relationship was shown to be more accurate for the effective binary diffusion of solute *j* in the mixture, D_j (43):

$$D_j \sqrt{\eta_{\mathrm{m}}} = x_{\mathrm{l,w}} D_{j,\mathrm{w}} \sqrt{\eta_{\mathrm{l,w}}} + x_{\mathrm{l,eth}} D_{j,\mathrm{eth}} \sqrt{\eta_{\mathrm{l,eth}}} \tag{26}$$

Here η_{m}, $\eta_{\mathrm{l,w}}$ and $\eta_{\mathrm{l,eth}}$ are the liquid viscosity of the mixture, water, and ethanol at the droplet temperature, respectively. $D_{j,\mathrm{w}}$ and $D_{j,\mathrm{eth}}$ are the binary diffusion coefficients of solute j in water and ethanol, respectively, which, if unknown, can be calculated using the Stokes-Einstein equation (44).

In this study, after the calculation of droplet temperature, evaporation rate and solvent compositions at the end of each time-step, Equation 25 is solved numerically to give the radial concentration distribution of each solute inside the droplet. These distribution profiles can then be used to find the relevant particle formation thresholds, such as the time to reach saturation, time to reach true density, etc (38).

Results and Discussions

Evaporation of Water/Ethanol Microdroplets

In order to study the accuracy and applicability of the two reviewed models, namely the Maxwell and Stefan-Fuchs models, mixtures of water and ethanol are considered due to their safety and their potential in the pharmaceutical industry for the spray-drying of inhalable microparticles. This mixture is specifically difficult to study numerically and experimentally because of its associated highly non-ideal behavior. The evaporation CK-EDB measurements of microdroplets of the pure solvents at two different temperatures and 0% relative humidity are compared with the two different models in Figure 2. These plots are normalized by the initial droplet diameter squared to permit the comparison of different sized droplets in a single figure (14). The experiments conducted with the CK-EDB had uncertainties in temperature and relative humidity of about ±1.5 °C and ±1%, respectively. The initial droplet diameters ranged from 40 to 52 μm in these experiments and, in all of the simulations in this study, the initial droplet temperature was equal to 20 °C, unless stated otherwise. In the experiments, the initial droplet diameters were obtained from retrograde extrapolation of a number of consecutive data points, as the diameter can only be measured using light scattering once the droplets are trapped inside the balance, not immediately upon generation. Typically, five experiments were conducted for each case resulting in the

error bars in Figure 2, calculated from the standard deviation of the size at each time point. These error bars do not account for the different uncertainties of the experimental procedure such as those caused by the temperature and relative humidity measurements. At these low ambient temperatures, the differences between the Maxwell and Stefan-Fuchs models are negligible. There is good agreement between both models and the experimental data, showing that both models are suitable for single solvent systems at low temperatures.

The evaporation curves of a mixture of 0.3:0.7 w/w water/ethanol at three different gas temperatures are compared in Figure 3. Good agreement is observed between the experimental and numerical data including the changes in the evaporation rates due to compositional variation of the droplets. There are small differences between the measured and simulated droplet diameters, which besides the experimental uncertainty, are likely due to the simplifications in the numerical model such as the well-mixed and quasi-steady assumptions, as well as the inaccuracies in the material properties and activity coefficients. Specifically, the time at which ethanol is depleted from the droplet, seen as the sharp change in the slope of the plots, is slightly overpredicted in the model. The evaporation histories for three different water and ethanol mixtures, all at 20 °C gas temperature, are shown in Figure 4(a). The point at which the evaporation rate is suddenly reduced, due to the ethanol depletion inside the droplet, is delayed by decreasing the water content to a point at which the behavior is reversed, and the evaporation rate displays an increasing trend as seen in the 0.2:0.8 w/w water/ethanol case. This reversal in behavior can be observed from both the experimental and numerical results in this figure. This phenomenon can also be seen from the predicted evolution of the water mass fraction as shown in Figure 4(b), in which the droplet evolves into a water-rich composition for the cases of lower ethanol content, while in the last case the opposite is observed. These observations point to an intermediate composition at which the mixture has a relatively constant fraction (14). This important scenario will be discussed in more detail below.

In actual spray-drying applications, the drying temperatures are much higher than those studied above. In order to confirm the validity of the model and compare the Maxwell and Stefan-Fuchs models at elevated

temperatures, evaporation histories of some mixtures of water and ethanol at 200 °C are compared to the numerical results of Lupo and Duwig (14) in Figure 5. The Stefan-Fuchs model shows close agreement with their results, even though there are two major differences between the models. First, they modeled the internal solvent and heat diffusion explicitly, while a well-mixed droplet is assumed here. Second, they used an average value for the vapor diffusion coefficient of different solvents, while we retain the diffusion coefficients of each specific vapor in Equation 18. These differences are suspected to be responsible for the small dissimilarities between their model and the Stefan-Fuchs model, while as expected the Maxwell model deviates more significantly. Even the Maxwell model over-predicts the evaporation rates by less than 20% at this high temperature, which in turn will over-predict the Péclet number by the same value. This over-prediction is likely an acceptable error in qualitative particle formation studies, considering the presence of other uncertainties. Hence, either model can be considered acceptable for most particle engineering studies aimed at process design.

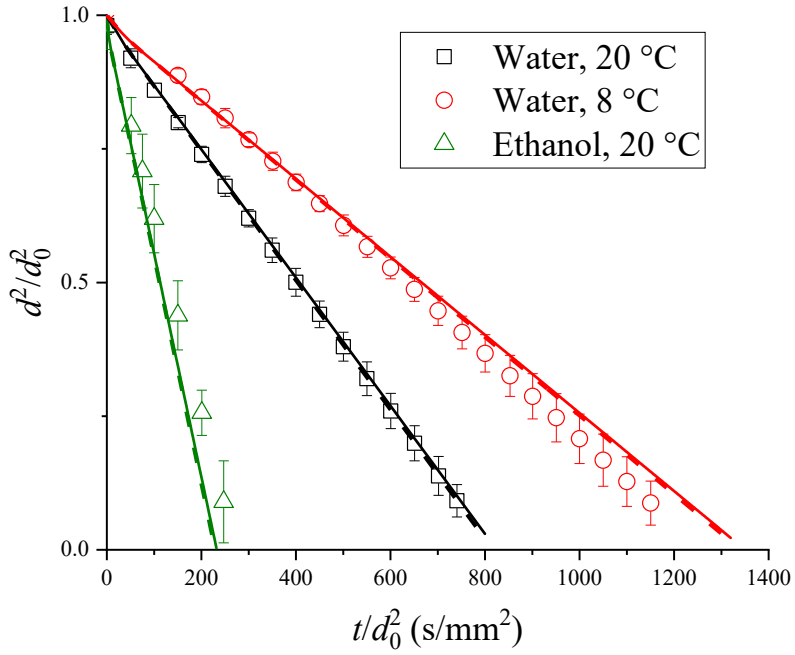

Figure 2 Evaporation histories of water and ethanol microdroplets at different temperatures and 0% RH. Symbols: Experimental CK-EDB data, solid lines: Stefan-Fuchs model, dashed lines: Maxwell model.

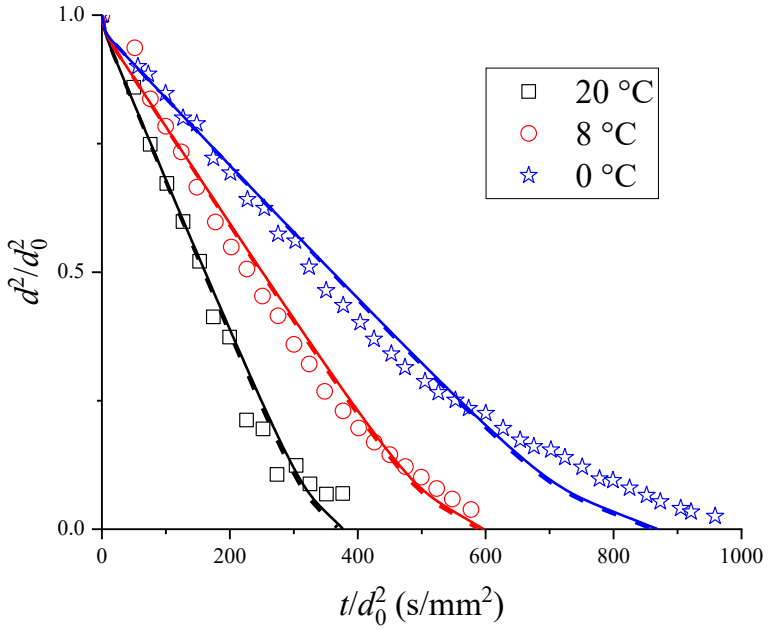

Figure 3 Evaporation histories of 0.3:0.7 w/w water/ethanol mixtures at three different temperatures. Symbols: Experimental CK-EDB data, solid lines: Stefan-Fuchs model, dashed lines: Maxwell model.

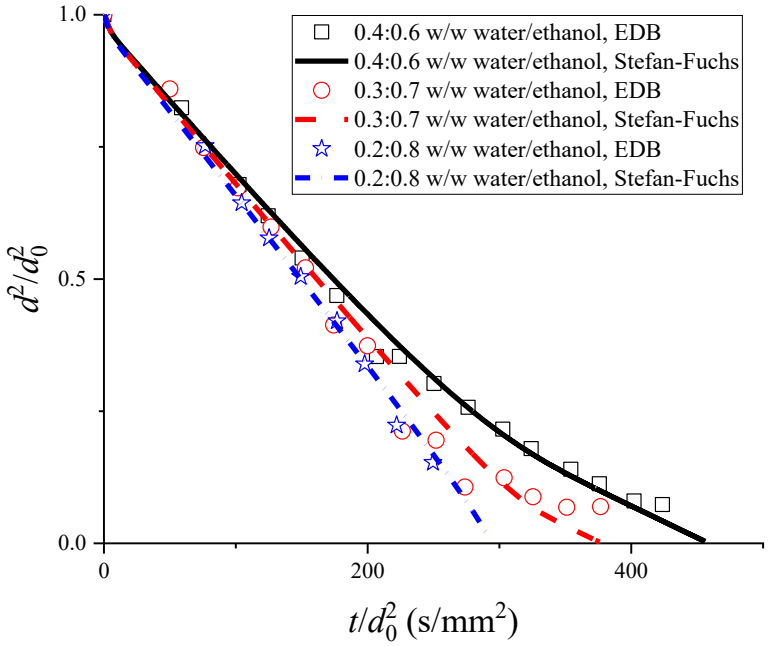

(a)

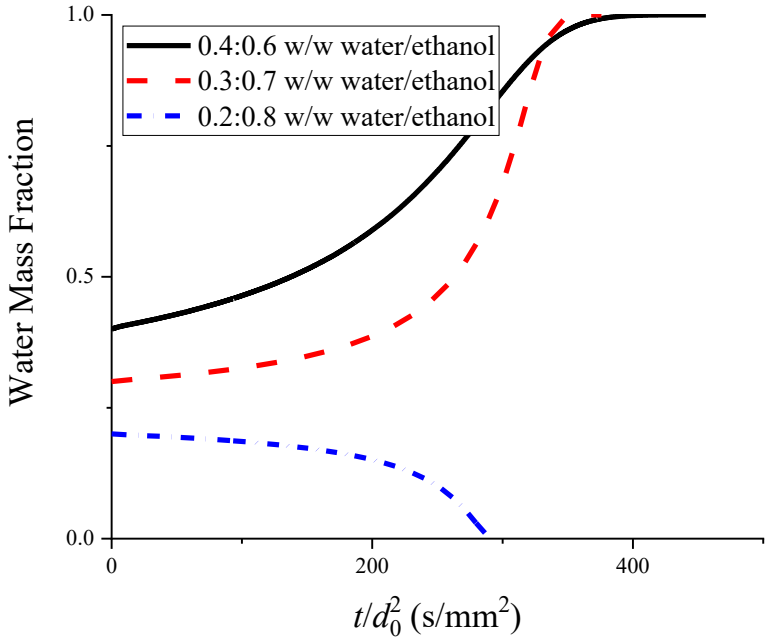

(b)

Figure 4 (a) Evaporation histories of three different compositions of water and ethanol at 20 °C, (b) their predicted water mass fraction histories.

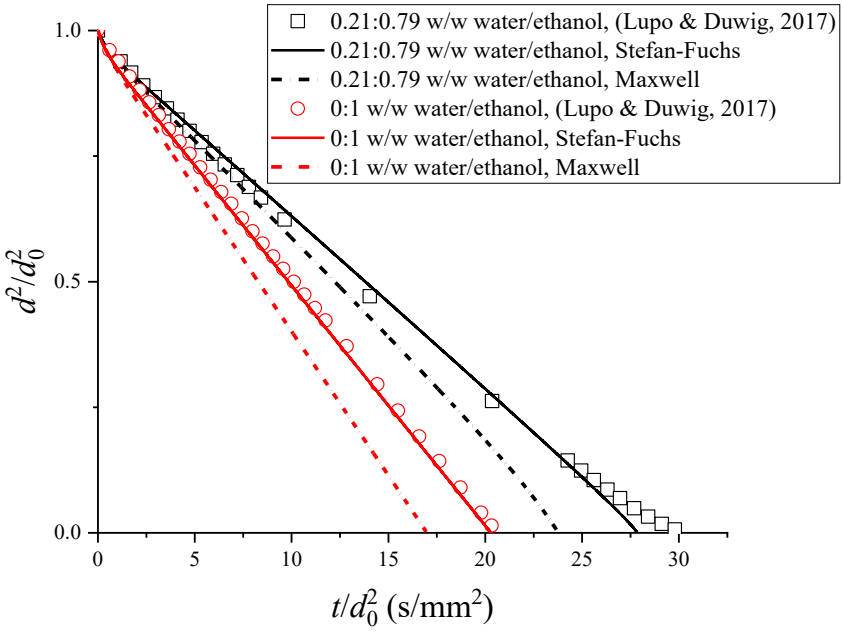

Figure 5 Evaporation histories of some water and ethanol mixtures using both the Stefan-Fuchs and Maxwell models compared to another numerical work at 200 °C (14).

Iso-Compositional Drying

It is well known in the distillation and boiling literature that the proportions of certain compositions of liquid mixtures remain constant during boiling. These specific compositions are called azeotropes of the mixture, whose vapors maintain the exact same composition during boiling (45). For example, a water/ethanol mixture at 101 kPa with 95.57% water by mass will boil at a constant temperature of 78.15 °C while maintaining this composition (46). An evaporating multicomponent droplet might also show similar behavior at a specific composition and ambient temperature, relative humidity and pressure, which conditions we shall collectively call the iso-compositional drying, with the composition of the droplet constant for the majority of the droplet's lifetime. The evaporation rate, the Péclet number, droplet

temperature, different solute solubilities and all other temperature- and composition-dependent properties of the droplet will also remain constant. These facts simplify the particle formation study, as the system behaves as a single-solvent solution and all the previous studies on the particle formation of such systems can be employed (11,26). It is worthwhile to note that this "iso-compositional" state might or might not happen for different solvents, as it is strongly related to the level of non-ideality of the components and their vapor pressures (47). For example for ideal mixtures, no possible iso-compositional evaporation of the droplet can be achieved at any temperature or composition as discussed in more detail in (47). For an evaporating droplet to be iso-compositional during drying, the following relationship must hold:

$$\frac{\dot{m}_i}{\dot{m}_\mathrm{t}} = y_{\mathrm{l},i}. \tag{27}$$

In other words, the fractional evaporation rate of each species should be equal to its mass fraction inside the droplet. Using Equations 18 and 27 and relating the surface vapor mass fractions to the liquid mass fractions, one can arrive at an implicit equation to solve for the specific iso-composition. However, the solution is complicated as the droplet temperature is unknown and therefore requires an iterative procedure. Alternatively, for the specific case of ethanol/water mixtures in this study, the initial droplet composition was varied to identify a nearly constant water composition during the drying to arrive at the iso-composition at the specific drying temperature and relative humidity. For example, the iso-composition at a drying temperature of 20 °C and in dry air was obtained using a plot similar to the one shown in Figure 6, which shows the dependence of the instantaneous water mass fraction normalized by the initial water fraction on the time normalized by the total drying time of the droplet. The initial mass fraction around the suspected iso-compositional point was varied by 0.1% to approximate this value accurate to ±0.1%. At these conditions, the iso-compositional water mass fraction is estimated to be about 23.7%. As seen from Figure 6, when the water content is less than the iso-compositional value, the water will evaporate completely before the ethanol, and there will be an increase in the ethanol content with time. The reverse is observed for water contents higher than the iso-compositional value. The same procedure was performed for other drying temperatures ranging from 10 °C to 200 °C and at 0% RH, all

with an initial droplet temperature of 20 °C. The iso-compositional mass fractions and the wet-bulb temperatures for this temperature range are shown in Figure 7. It is observed that the iso-composition is relatively constant and equal to 23.7% between 10 °C and 40 °C with a small decrease above this temperature range reaching a value equal to 22.6% at 200 °C. This small variation of the iso-compositional fractions with temperature simplifies the formulation design in an actual spray-dryer, whose drying gas temperature gradients are generally large. The droplet temperature or the wet-bulb temperature also increases steadily with a decreasing slope when the drying gas temperature is increased. Even at a drying gas temperature of 200 °C, a typical maximum temperature for the spray drying of pharmaceuticals, the droplet temperature is only about 34 °C due to the evaporative cooling—well below the boiling temperature of the azeotrope of water and ethanol at atmospheric pressure, which is about 78.15 °C. This fact encouraged the use of the term “iso-compositional point” instead of the “azeotropic point” in this study.

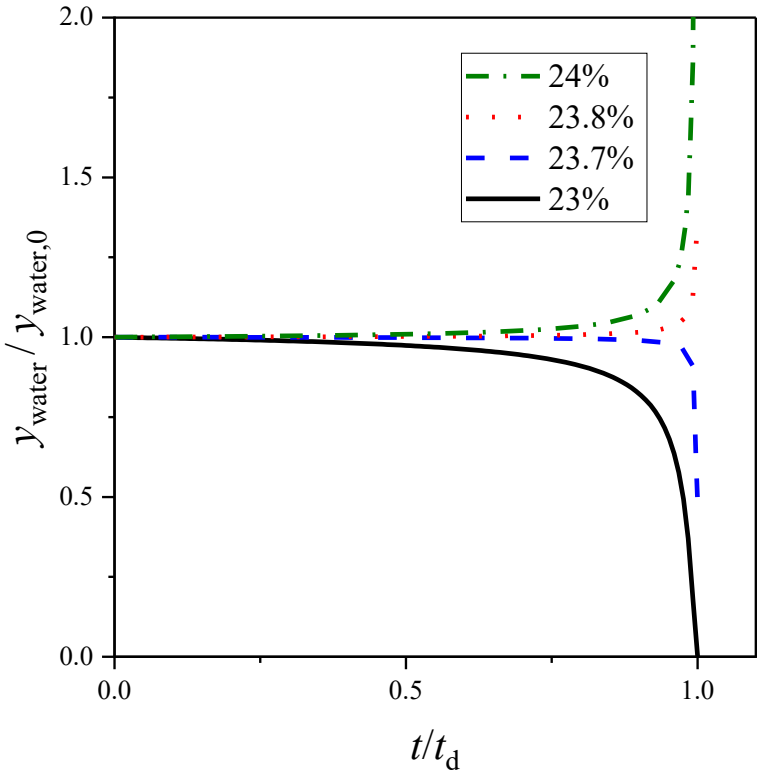

Figure 6 The composition variation of a water/ethanol droplet with different initial water mass fractions in dry air at 20 °C, used to find the iso-compositional point.

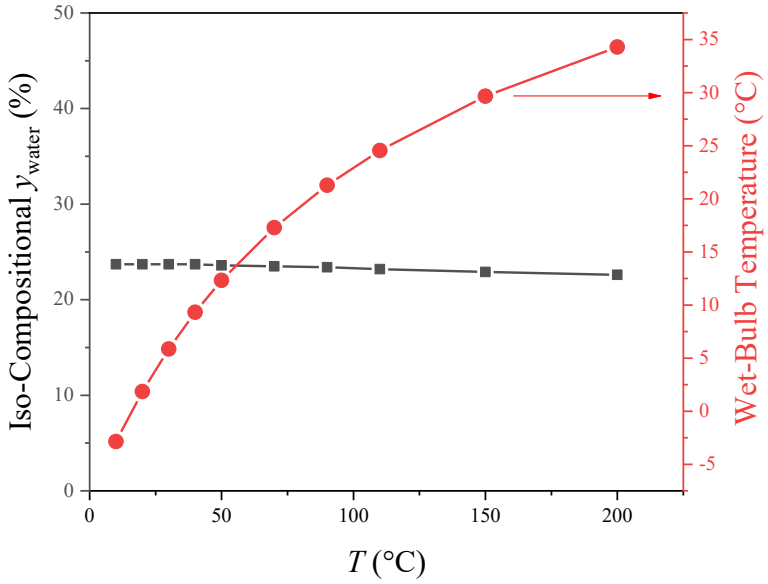

Figure 7 The iso-compositional water mass fractions of water/ethanol mixtures and the corresponding droplet temperatures at different drying temperatures in dry air.

The evaporation rates, κ, of the water/ethanol mixtures at the calculated iso-compositions, accompanied by the evaporation rates of the pure solvents, are shown in Figure 8. It is also observed that the evaporation rate at the iso-compositional point is approximately equal to the molar weighted average of the evaporation rates of pure water and ethanol at the respective drying temperature.

Spray-drying in iso-compositional conditions holds some advantages during the formulation and process design of pharmaceutical aerosols, where predicting the evaporation rates of the solution droplets is an important step (11,26). First, as mentioned before, temperature, composition and all the dependent properties such as the solubility values of the solutes are constant, greatly simplifying the calculations pertaining to particle design. Furthermore, some of the hydrophobic corticosteroids such as beclometasone dipropionate (BDP) and budesonide (BUD) have a maximum solubility close to this iso-composition in water/ethanol mixtures as shown in Figure 9. For BDP the solubility at the iso-composition is about 40% greater than that in pure ethanol, while for BUD this increase is about 10%. Hence, for a given initial droplet size, a single spray-dried particle of BUD or BDP at the iso-composition can contain 40% and 10% more mass of the actives, respectively, than a particle spray-dried in pure ethanol.

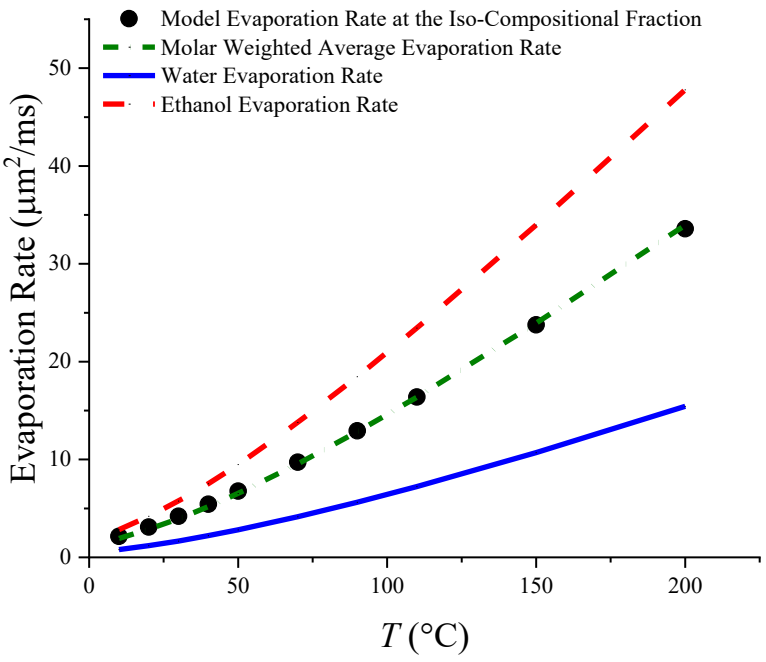

Figure 8 The evaporation rates, κ, of water/ethanol mixtures at the iso-compositional point compared to those of pure components and the molar weighted average.

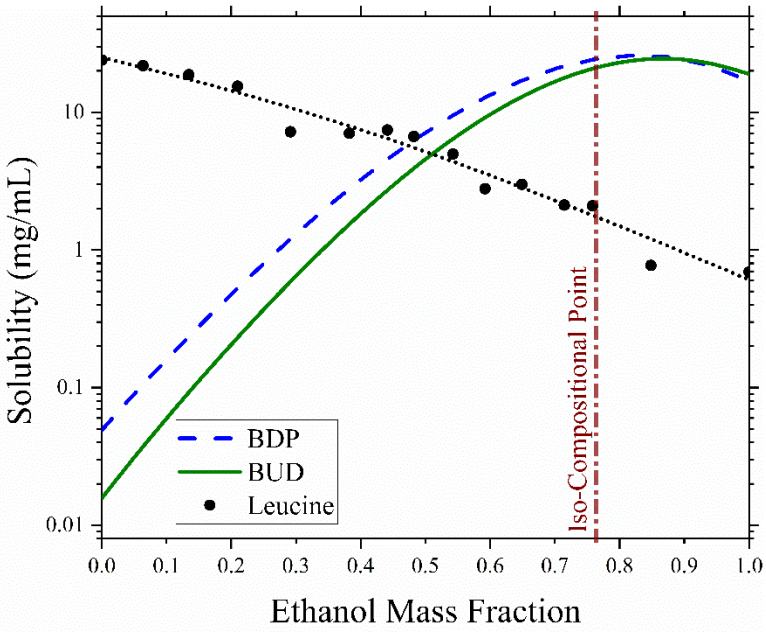

Figure 9 Equilibrium solubility values of beclometasone dipropionate (BDP), budesonide (BUD) and leucine in water/ethanol mixtures at 25 °C. The BDP and BUD solubilities are predicted using the Jouyban-Acree model (48), while the leucine solubility is from (8).

BUD and BDP are usually spray-dried from ethanol or ethanol/water mixtures because of the low solubility of these actives in water. Spray-drying of these drugs in the absence of any shell former will produce amorphous or semi-amorphous particles with a smooth and rather cohesive surface (8,49,50). The cohesive nature of the resulting particles reduces their manufacturing and aerosolization efficiencies. To address this problem, different shell formers can be employed, e.g. to increase the rugosity of the particles. A shell former is an excipient that precipitates early during droplet evaporation and then forms a shell around the internal actives and excipients. These shells are often crystalline or rugose and can lower the cohesive forces between the particles. Leucine is considered in this study as a shell former candidate which has been used to make a shell around the actives in the center of the particles in order to increase production yield, dispersibility, and long-term storage stability of the final product (38,51). Unlike hydrophobic drugs, leucine has a higher solubility in water and very small solubility in alcohols, as shown

in Figure 9. Hence the required fraction of the shell former should also be taken into consideration during the design stage of the formulation and the co-solvent system. This is specifically more important for leucine because it may produce different solid phases at different solid fractions (51). A completely crystalline leucine shell is preferred, as small amounts of amorphous leucine in the presence of crystalline leucine may affect the long-term stability of the product.

Particle Formation in Co-solvent Systems

The internal profiles of the dried particles play an important role in the resulting properties of the product. As previously noted, the behavior of solutes inside an evaporating droplet can be characterized by the Péclet number, which is constant in a single solvent droplet (considering the composition-dependent diffusion coefficient) but varies with time in a multi-solvent system. During the drying process of a multi-solvent system, the evaporation rate and the effective diffusion coefficients generally change with time, and thus the Péclet number varies accordingly, as seen from Equation 23. Hence, as opposed to reaching the steady-state value characteristic of pure solvent cases, the surface enrichment evolves in a way that cannot be predicted by the steady state model.

How much the change in evaporation rate, solvent composition and solute solubility will affect particle formation depends on the type of excipient: As a first example, the internal solute diffusion of trehalose, a typical disaccharide glass former used as a stabilizer for biologics, in different compositions of water and ethanol at 80 °C is modelled here and the predicted time dependence of the Péclet number and surface enrichment, E_s, are reported in Figure 10. The Péclet numbers of trehalose in pure water and pure ethanol reach constant values of 1.0 and 4.3, respectively. The initial change in evaporation rates and thus the Péclet number is due to the equilibration of the droplet temperature, as the initial droplet temperature is 20 °C in all of the simulated cases. The surface enrichment of the single solvent cases reaches the steady-state values as predicted by the VFL model shown in Equation 24. The value predicted by the VFL model

is the final surface enrichment, reached after a transient stage (discussed in more detail in (11)). Iso-compositional drying is observed for droplets with a composition of 0.23:0.77 w/w water/ethanol and, as expected, the system behaves like a single solvent, with a steady Péclet number and surface enrichment converging to a steady value. In the other cases, with 0.3:0.7 and 0.7:0.3 w/w water/ethanol, the Péclet number starts at intermediate values and eventually reaches that of pure water. This is expected as the mass fraction of water increases over time, a consequence of initial water mass fractions that are higher than the iso-compositional value. The Péclet number of the 0.3:0.7 w/w water/ethanol case and the droplet composition are relatively constant throughout most of the drying time, a consequence of an initial composition close to the iso-composition. The surface enrichment for this case increases and reaches the stable value of ~1.9 with the initially constant Péclet number of ~4.0, but then falls abruptly as the ethanol content in the droplet is depleted and converges to the steady state surface enrichment of pure water. The surface enrichment of the 0.7:0.3 w/w water/ethanol case reaches a maximum at about 20% of the droplet lifetime and then gradually decreases to reach the steady value of pure water. Precipitation is not considered in these calculations; in reality, solid particles might be formed well in advance of the predicted final drying times depending on the initial amount of dissolved solids. This is especially true for shell formers and crystallizing solutes which might crystallize or precipitate on the surface, with a liquid phase remaining near the center of the particle. Indeed, the process could be designed to create an iso-compositional-like state using solvent compositions close to the actual iso-composition with precipitation occurring before the abrupt change in composition as seen in the 0.3:0.7 w/w water/ethanol case in Figure 10. Such a process would take advantage of drying at constant evaporation rates.

In the specific example of trehalose, the solute enrichment at the particle surface in ethanol is only double that of water; hence diffusion alone is unlikely to cause severe morphological differences. It has been shown previously that spray-dried particles from different co-solvent compositions can produce particles of significantly different aerosol performance and morphologies (8,52,53). In all of these previous studies, the solid component that contributed to the change in morphology showed different crystallization

behavior at different solvent compositions. For an excipient that rarely crystallizes during spray-drying and has relatively similar Péclet numbers in the solvents of interest, such as trehalose, the change of solvent and solvent compositions does not strongly alter the general particle morphology. This can be seen from the Field Emission Scanning Electron Microscopy (FESEM) images shown in Figure 11. These trehalose particles were collected using the monodisperse droplet chain instrument for pure water and 0.30:0.70 w/w water/ethanol at 80 °C drying temperature. The initial feed concentration was 100 mg/mL in pure water and 10 mg/mL in the co-solvent case, due to solubility limitation. The internal structure of a single trehalose particle from the co-solvent case, cut by a Focused Ion Beam (FIB) under a Helium Ion Microscope (HIM), is also observed in the inset figure, which confirms a solid structure throughout the radial direction, similar to that of spray-dried trehalose in pure water (26). Based on these observations it can be concluded that the general particle morphology of trehalose, which usually forms an amorphous solid during spray-drying, is similar between these two cases. Hence, previous experience with aqueous systems can be employed for particle design of trehalose containing formulations in ethanol/water solvent systems.

On the other hand, if there is an excipient in the formulation that can either crystallize during spray-drying (with possibly different crystallization kinetics in different solvents), or has significantly different Péclet numbers in different solvents, or shows noticeably different surface activity behavior in different solvents, then the particle morphology is expected to vary with any change in composition of the co-solvent system. To illustrate this theory, leucine particles were generated in the monodisperse droplet chain setup at 20 °C with an initial concentration of 0.5 mg/mL in different initial water and ethanol compositions of 1.00:0.00, 0.75:0.25, 0.50:0.50 and 0.25:0.75 w/w water/ethanol, noting that the last case is close to the iso-compositional point of the co-solvent system. The FESEM micrographs of the collected particles are shown in Figure 12. Significant changes in morphology are observed with increasing initial ethanol content. First, the volume equivalent diameter of the particles increases with increasing ethanol content. The lower solubility of leucine and the higher Péclet number in ethanol compared to water initiates shell

formation at an earlier point in the evaporation process and at a larger diameter. Second, the general surface properties of the particles look similar for the first three cases, with an outer shell and a single dimple, but are substantially different in the case with the highest amount of ethanol content with particles exhibiting a porous structure throughout. A higher resolution micrograph of one of the particles from the 0.25:0.75 w/w water/ethanol case was obtained using Helium Ion Microscopy (HIM). The particle was cut using a Focused Ion beam (FIB) to verify its porous internal structure. The results are shown in Figure 13.

In order to understand and explain these changes in morphology, the numerical model was used to predict the evaporation histories using the experimental conditions and for initial leucine concentrations of 0.5 and 1.5 mg/mL. As leucine can crystallize during spray-drying (51), the available time for crystallization after reaching saturation, $t_{\mathrm{final}} - t_{\mathrm{sat}}$, is an important parameter in determining the precipitation dynamics (11,26), in which t_{final} is the total evaporation time of the droplet and t_{sat} is the time at which the solute reaches saturation. The dimensionless values of the available time for crystallization after reaching saturation $\tau_{\mathrm{c}} = 1 - \frac{t_{\mathrm{sat}}}{t_{\mathrm{final}}}$ are shown in Figure 14(a). τ_{c} is seen to gradually increase with increasing initial ethanol content for both concentrations, with a sharp increase at about 65% and 55% ethanol fractions for the 0.5 mg/mL and 1.5 mg/mL cases, respectively. This increase in τ_{c} is a consequence of the dependence of t_{sat} on the solubility, which is smaller for leucine in ethanol than in water. Also, τ_{c} is longer for the 1.5 mg/mL case since a higher solid concentration means an earlier saturation and a longer time available for crystallization to occur. The general increasing trend in τ_{c} is responsible for the larger particle diameters with increasing ethanol content observed from the experiments, since earlier crystallization means precipitation in a larger droplet. The iso-compositional point of the co-solvent system is close to 77% by mass of ethanol, and leucine solubility is much lower in ethanol than in water, as seen in Figure 9. Hence, the abrupt increase of τ_{c} is due to the occurrence of saturation in a pure water droplet before the abrupt change, as opposed to saturation in a water and ethanol mixture after this point. This can be seen from the mass fraction of ethanol left in the droplet at

the time of saturation, $y_{\mathrm{ethanol,sat}}$, versus drying time, as shown in Figure 14(b). It is seen that at lower initial ethanol contents, leucine reaches saturation in pure water as these conditions are well below the iso-compositional point, and the droplet loses its ethanol fraction quickly as discussed earlier. At initial ethanol fractions of about 60% and 50% for the 0.5 mg/mL and 1.5 mg/mL cases, respectively, $y_{\mathrm{ethanol,sat}}$ starts to rise, pointing to possible change in the crystallization kinetics as also indicated by the sharp increase in the τ_c plot. Some sample particles of the respective cases are also shown in Figure 14(b) to compare the change in the morphology of the leucine particles to $y_{\mathrm{ethanol,sat}}$. It is seen that when leucine reaches saturation while a small fraction of ethanol is present, the overall morphology of the particles is similar, but saturation during the presence of significant amounts of ethanol causes clear morphological differences. This variance can explain previously published observations that increasing the initial ethanol content above a certain limit increases the dispersibility and process yield of spray-dried budesonide particles with leucine as a shell former (8).

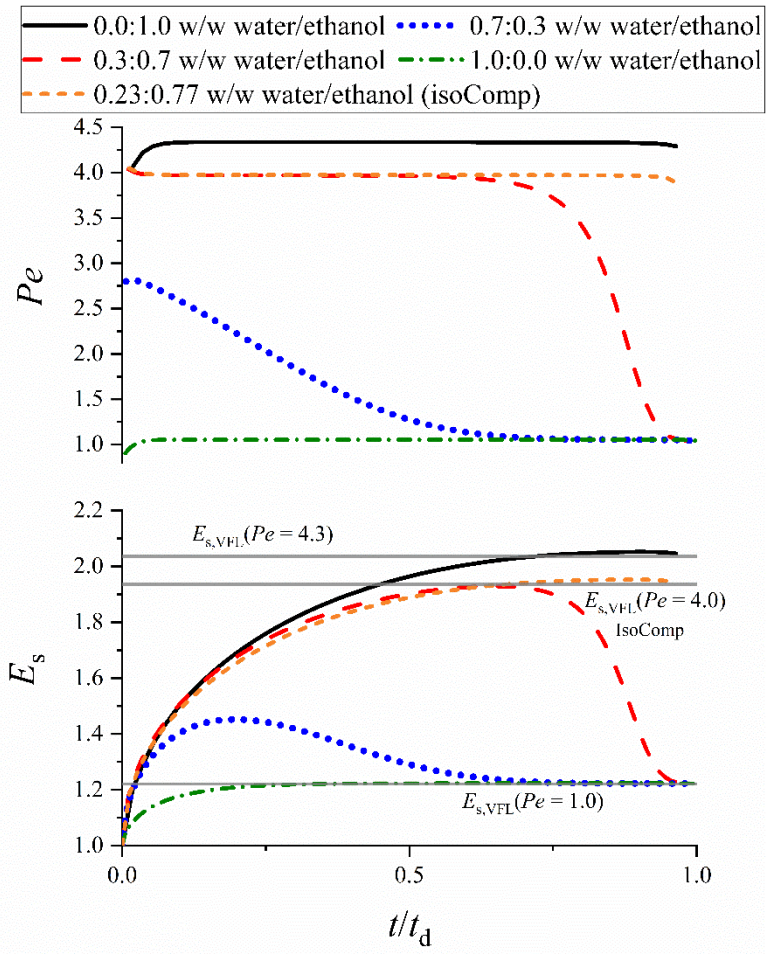

Figure 10 Histories of Péclet number and surface enrichment of trehalose at different compositions of water and ethanol drying at a gas temperature of 80 °C.

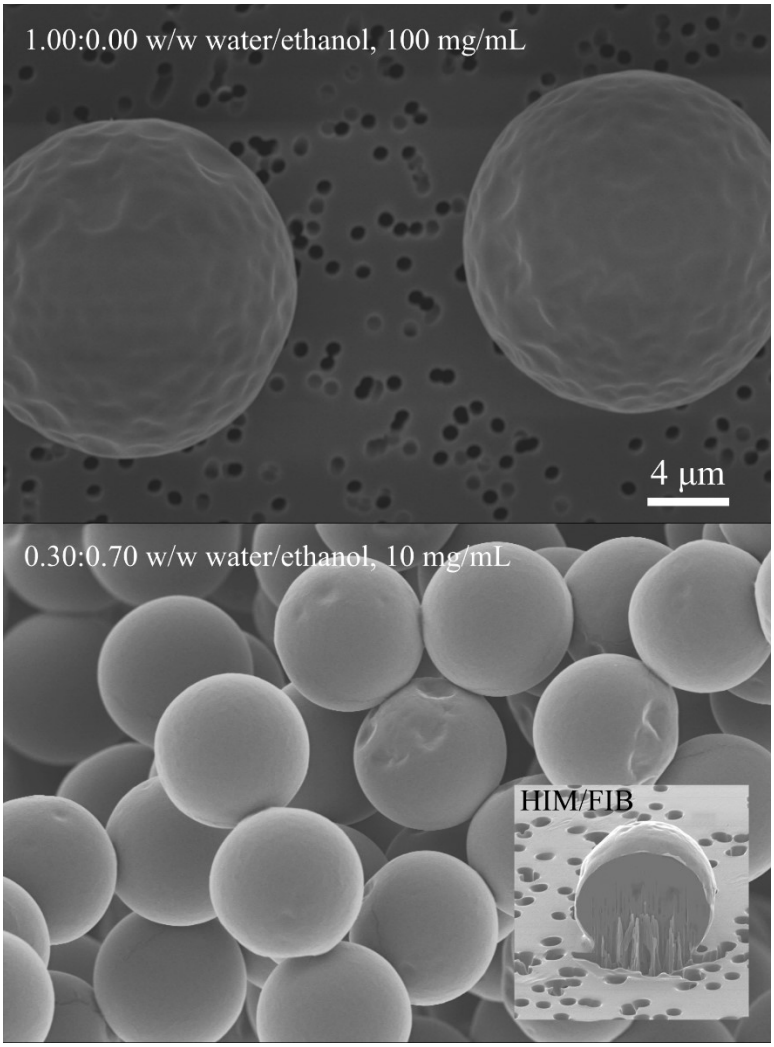

Figure 11 Trehalose particles collected from the monodisperse droplet chain instrument all at 80 °C. Top figure: 100 mg/mL in pure water, Bottom figure: 10 mg/mL in a mixture of water and ethanol and a sample HIM/FIB cut particle in the inset figure. The scale bar applies to all three figures.

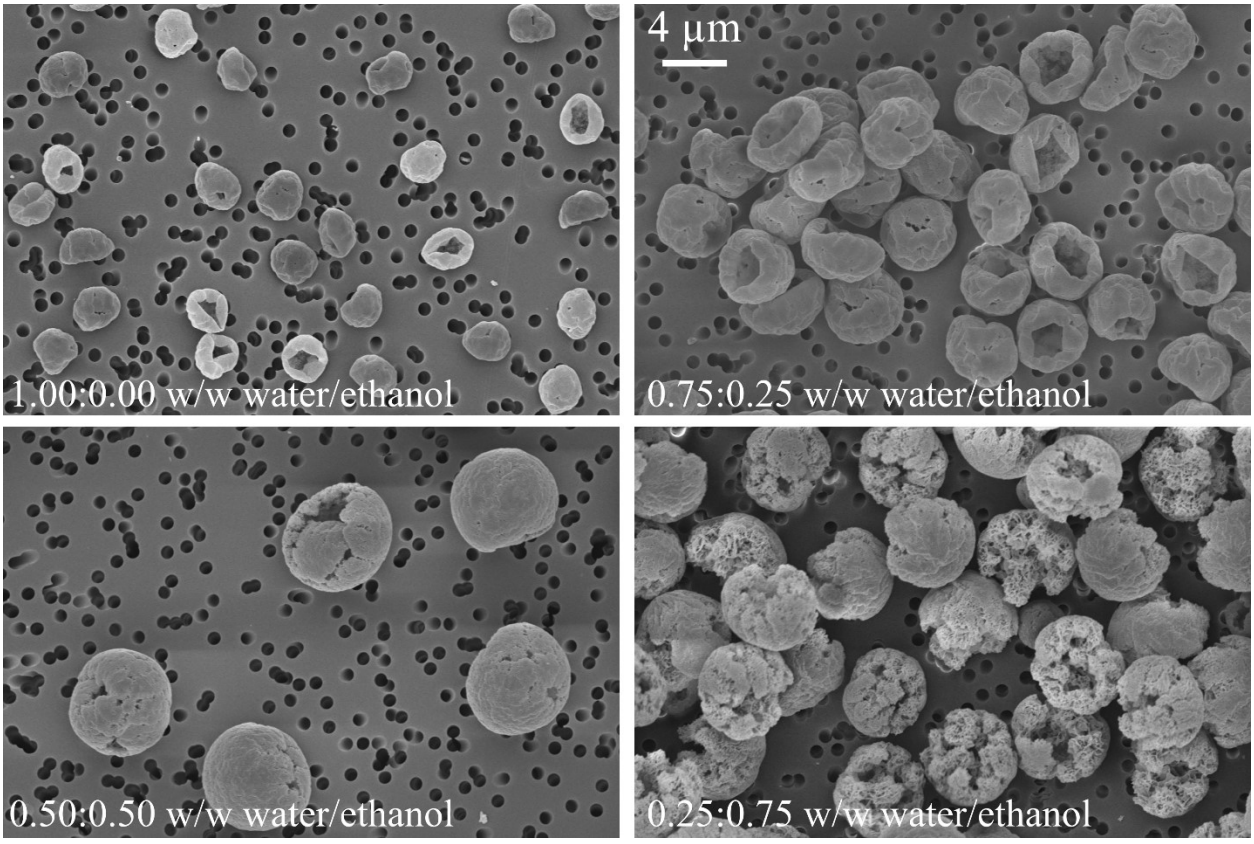

Figure 12 Monodisperse leucine particles collected from the droplet chain instrument dried at 20 °C from a solution of 0.5 mg/mL of different water and ethanol compositions.

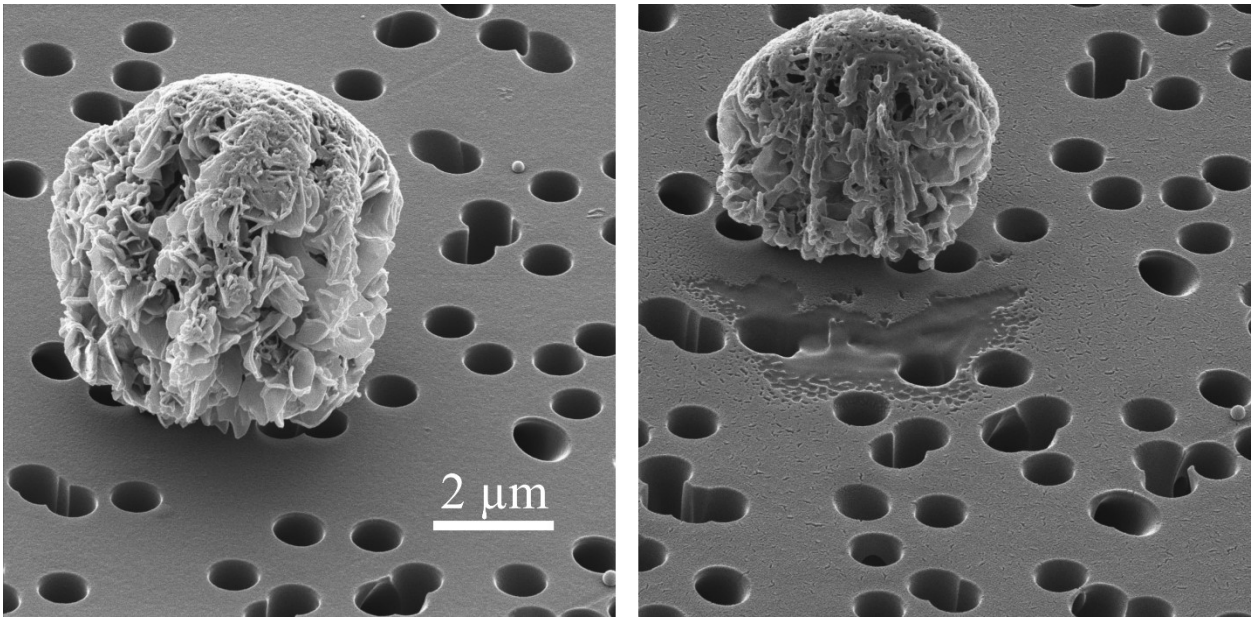

Figure 13 HIM images of a leucine particle dried at 20 °C from a solution of 0.5 mg/mL with 0.25:0.75 w/w water/ethanol initial co-solvent ratios. Left panel: uncut particle, Right panel: cut particle.

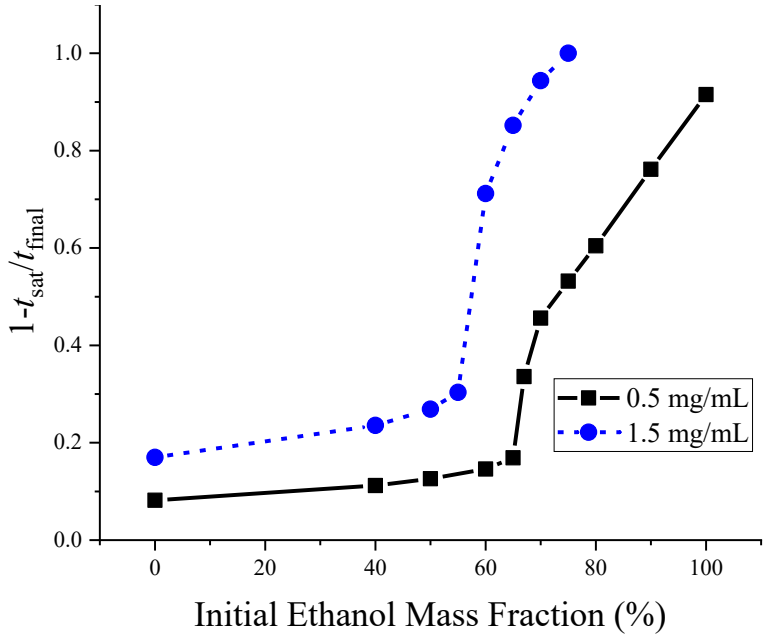

(a)

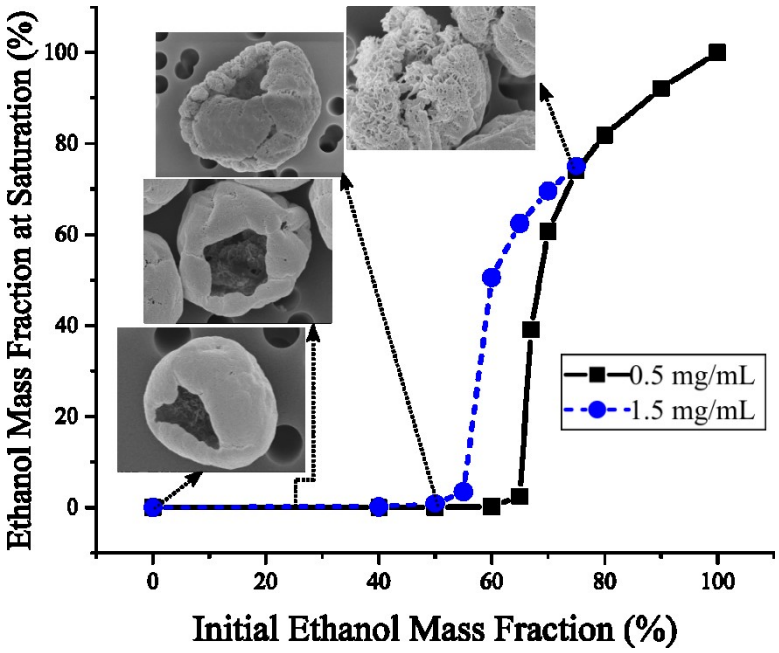

(b)

Figure 14 Numerical results for different concentrations of leucine drying at 20 °C in a range of initial water and ethanol compositions. (a) Dimensionless available time for crystallization, τ_c, (b) amount of ethanol left at saturation, $y_{ethanol,sat}$ accompanied by samples of collected leucine particles with initial concentration of 0.5 mg/mL.

Conclusion

Spray-drying of inhalable pharmaceutics from co-solvent systems is more complex than it is for pure solvents because of temporal and droplet-size dependent variations in the evaporation rate, solubility, and crystallization kinetics. In such systems, the morphology of the particles – and consequently the performance of the dosage form – is sensitive to co-solvent ratio and other formulation and process parameters. This additional complexity heightens the need for numerical modeling during product development, e.g. when choosing initial processing conditions or during scale-up. Here, both the Maxwell and the Stefan-Fuchs models were used to study the evaporation kinetics of multi-solvent droplets in conjunction with appropriate methods of solving internal diffusion equations for particle formation applications. The Stefan-Fuchs model is most accurate at higher temperatures but is more complex and requires knowledge of more transport properties, while the Maxwell model can accurately be used at low temperatures with minimal complexity.

Exploring a variety of water/ethanol systems with different actives and excipients (trehalose, leucine), we find that co-solvent droplets can exhibit azeotropic-like behavior during evaporation at specific compositions, which we refer to as iso-compositional. We also find that the iso-compositional point in a water ethanol co-solvent system is a weak function of the drying temperature at drying conditions typical for spray drying. For a water/ethanol droplet, the evaporation rate at the iso-compositional point can be obtained from the molar weighted average of the evaporation rates of the pure components at any specified drying temperature. At the iso-compositional point the particle formation resembles that of a pure solvent case, and simple analytical particle formation models such as the VFL model can be used. The effect of relative humidity on the existence or composition of the iso-compositional state has not been analyzed and will be considered in later studies as even small amounts of ambient humidity can alter the vapor-liquid-equilibrium of the system.

Finally, we find that for non-crystallizing excipients for which particle formation is mostly diffusion controlled and the Péclet number is relatively similar in different co-solvent systems (e.g. trehalose), the

morphologies of the dried particles are likely similar to those formed using water alone. This similarity allows experience from aqueous systems to be transferred to co-solvent systems for these excipients. In contrast, the presence of crystallizing components with large solubility differences in different co-solvent compositions (e.g. leucine) will likely exhibit noticeably different particle morphologies. A detailed knowledge of crystallization kinetics and solubility data is then required for such systems in order to explain and understand the source of these differences. This methodology can then be applied to a practical system of interest containing multiple active pharmaceutical ingredients and excipients.

Acknowledgments

Reinhard Vehring acknowledges support for this work from the Natural Sciences and Engineering Research Council of Canada, grant RGPIN-2016-04111 and Jonathan Reid and Florence Gregson acknowledge that the experimental work on the electrodynamic balance was supported by the Engineering and Physical Sciences Research Council under grant code EP/N025245/1.

1. References

1. Haddrell AE, Davies JF, Miles REH, Reid JP, Dailey LA, Murnane D. Dynamics of aerosol size during inhalation: Hygroscopic growth of commercial nebulizer formulations. Int J Pharm. 2014 Mar 10;463(1):50–61.

2. Rovelli G, Miles REH, Reid JP, Clegg SL. Accurate Measurements of Aerosol Hygroscopic Growth over a Wide Range in Relative Humidity. J Phys Chem A. 2016 Jun 30;120(25):4376–88.

3. Cai B, Tuo X, Song Z, Zheng Y, Gu H, Wang H. Modeling of spray flash evaporation based on droplet analysis. Appl Therm Eng. 2018 Feb 5;130:1044–51.

4. Brewster MQ. Evaporation and condensation of water mist/cloud droplets with thermal radiation. Int J Heat Mass Transf. 2015 Sep 1;88:695–712.

5. Sazhin SS. Modelling of fuel droplet heating and evaporation: Recent results and unsolved problems. Fuel. 2017 May 15;196:69–101.

6. Arpagaus C, Collenberg A, Rütti D, Assadpour E, Jafari SM. Nano spray drying for encapsulation of pharmaceuticals. Int J Pharm. 2018 Jul 30;546(1–2):194–214.

7. Chalvatzaki E, Lazaridis M. A dosimetry model of hygroscopic particle growth in the human respiratory tract. Air Qual Atmos Heal. 2018 May 1;11(4):471–82.

8. Boraey MA, Hoe S, Sharif H, Miller DP, Lechuga-Ballesteros D, Vehring R. Improvement of the dispersibility of spray-dried budesonide powders using leucine in an ethanol–water cosolvent system. Powder Technol. 2013 Feb 1;236:171–8.

9. Kauppinen A, Broekhuis J, Grasmeijer N, Tonnis W, Ketolainen J, Frijlink HW, et al. Efficient production of solid dispersions by spray drying solutions of high solid content using a 3-fluid nozzle. Eur J Pharm Biopharm. 2018 Feb 1;123:50–8.

10. Ivey JW, Bhambri P, Church TK, Lewis DA, McDermott MT, Elbayomy S, et al. Humidity affects the morphology of particles emitted from beclomethasone dipropionate pressurized metered dose inhalers. Int J Pharm. 2017 Mar 30;520(1–2):207–15.

11. Boraey MA, Vehring R. Diffusion controlled formation of microparticles. J Aerosol Sci. 2014 Jan;67:131–43.

12. Grasmeijer N, Frijlink HW, Hinrichs WLJ. Model to predict inhomogeneous protein–sugar distribution in powders prepared by spray drying. J Aerosol Sci. 2016 Nov 1;101:22–33.

13. Widmann JF, Davis EJ. Evaporation of multicomponent droplets. Aerosol Sci Technol. 1997;27(2):243–54.

14. Lupo G, Duwig C. A Numerical Study of Ethanol–Water Droplet Evaporation. J Eng Gas Turbines Power. 2017 Oct 3;140(2):021401.

15. Tonini S, Cossali GE. A multi-component drop evaporation model based on analytical solution of Stefan–Maxwell equations. Int J Heat Mass Transf. 2016 Jan 1;92:184–9.

16. Tonini S, Cossali GE. A novel formulation of multi-component drop evaporation models for spray applications. Int J Therm Sci. 2015 Mar 1;89:245–53.

17. Kuchma AE, Shchekin AK, Martyukova DS. The Stefan outflow in a multicomponent vapor–gas atmosphere around a droplet and its role for cloud expansion. J Aerosol Sci. 2016;102:72–82.

18. Fuchs NA. Evaporation and droplet growth in gaseous media. Oxford: The Pergamon Press; 1959.

19. Learoyd TP, Burrows JL, French E, Seville PC. Modified release of beclometasone dipropionate from chitosan-based spray-dried respirable powders. Powder Technol. 2008 Nov 20;187(3):231–8.

20. Ozyazici M, Yurdasiper A, Arici M. Triamcinolone acetonide dry powder inhalation: A new approach for treathing asthma. J Pharm Drug Deliv Res. 2016;5(6).

21. Khandouzi F, Daman Z, Gilani K. Optimized particle engineering of fluticasone propionate and salmeterol xinafoate by spray drying technique for dry powder inhalation. Adv Powder Technol. 2017 Feb 1;28(2):534–42.

22. Knox KJ, Reid JP, Hanford KL, Hudson AJ, Mitchem L. Direct measurements of the axial displacement and evolving size of optically trapped aerosol droplets. J Opt A Pure Appl Opt. 2007 Aug 1;9(8):S180–8.

23. Davies JF, Haddrell AE, Reid JP. Time-Resolved Measurements of the Evaporation of Volatile Components from Single Aerosol Droplets. Aerosol Sci Technol. 2012 Jun 1;46(6):666–77.

24. Baldelli A, Boraey MA, Nobes DS, Vehring R. Analysis of the Particle Formation Process of Structured Microparticles. Mol Pharm. 2015 Aug 3;12(8):2562–73.

25. Baldelli A, Power RM, Miles REH, Reid JP, Vehring R. Effect of crystallization kinetics on the properties of spray dried microparticles. Aerosol Sci Technol. 2016 Jul 2;50(7):693–704.

26. Vehring R, Foss WR, Lechuga-Ballesteros D. Particle formation in spray drying. J Aerosol Sci. 2007;38(7):728–46.

27. Kulmala M, Vesala T, Wagner PEE. An analytical expression for the rate of binary condensational particle growth: Comparison with numerical results. J Aerosol Sci. 1992 Jan 1;23(SUPPL. 1):133–6.

28. Finlay WH. The Mechanics of Inhaled Pharmaceutical Aerosols: an Introduction. 2nd ed. Elsevier; 2019.

29. Tonini S, Cossali GE. An analytical model of liquid drop evaporation in gaseous environment. Int J Therm Sci. 2012 Jul 1;57:45–53.

30. Periasamy Ravindran E, Davis J. Multicomponent evaporation of single aerosol droplets. J Colloid Interface Sci. 1982 Jan;85(1):278–88.

31. Newbold FR, Amundson NR. A model for evaporation of a multicomponent droplet. AIChE J. 1973 Jan 1;19(1):22–30.

32. Abramzon B, Sirignano WA. Droplet vaporization model for spray combustion calculations. Int J Heat Mass Transf. 1989 Sep 1;32(9):1605–18.

33. Hopkins RJ, Reid JP. A Comparative Study of the Mass and Heat Transfer Dynamics of Evaporating Ethanol/Water, Methanol/Water, and 1-Propanol/Water Aerosol Droplets. J Phys Chem B. 2006 Feb 1;110(7):3239–49.

34. Seinfeld JH, Pandis SN. Atmospheric Chemistry and Physics : From Air Pollution to Climate Change. New York, UNITED STATES: John Wiley & Sons, Incorporated; 2016.

35. Sirignano WA. Fluid dynamics and transport of droplets and sprays. Cambridge university press; 1999.

36. Gebreyohannes S, Neely BJ, Gasem KAM. One-parameter modified nonrandom two-liquid (NRTL) activity coefficient model. Fluid Phase Equilib. 2014 Oct 15;379:196–205.

37. Khattab IS, Bandarkar F, Fakhree MAA, Jouyban A. Density, viscosity, and surface tension of water+ethanol mixtures from 293 to 323K. Korean J Chem Eng. 2012 Jun 18;29(6):812–7.

38. Vehring R. Pharmaceutical particle engineering via spray drying. Vol. 25, Pharmaceutical Research. 2008. p. 999–1022.

39. Ekdawi-Sever N, de Pablo JJ, Feick E, von Meerwall E. Diffusion of Sucrose and α,α-Trehalose in Aqueous Solutions. J Phys Chem A. 2003 Feb 1;107(6):936–43.

40. Taylor R, Krishna R. Multicomponent mass transfer. Vol. 2. John Wiley & Sons; 1993.

41. Wilke CR. Diffusional properties of multicomponent gases. Chem Eng Prog. 1950;46(2):95–104.

42. Fairbanks DF, Wilke CR. Diffusion Coefficients in Multicomponent Gas Mixtures. Ind Eng

Chem. 1950 Mar 1;42(3):471–5.

43. Tang YP, Himmelblau DM. Effective binary diffusion coefficients in mixed solvents. AIChE J. 1965 Jan;11(1):54–8.

44. Bird RB, Stewart WE, Lightfoot EN. Transport Phenomena. Revised 2n. New York: John Wiley & Sons; 2006.

45. Smith JM, Van Ness HC, Abbott MM. Introduction to Chemical Engineering Thermodynamics. 7th ed. New York: McGraw-Hill; 2005.

46. Horsley LH. Table of Azeotropes and Nonazeotropes. Anal Chem. 1947 Aug 19;19(8):508–600.

47. Bader A, Keller P, Hasse C. The influence of non-ideal vapor–liquid equilibrium on the evaporation of ethanol/iso-octane droplets. Int J Heat Mass Transf. 2013 Sep;64:547–58.

48. Jouyban A, Acree WE. In silico prediction of drug solubility in water-ethanol mixtures using Jouyban- Acree model. J Pharm Pharm Sci (www cspsCanada.org). 2006;9(2):262–9.

49. D'Sa DJ, Lechuga-Ballesteros D, Chan HK. Isothermal Microcalorimetry of pressurized systems I: A rapid method to evaluate pressurized metered dose inhaler formulations. Pharm Res. 2014;31(10):2716–23.

50. Tajber L, Corrigan DO, Corrigan OI, Healy AM. Spray drying of budesonide, formoterol fumarate and their composites—I. Physicochemical characterisation. Int J Pharm. 2009 Feb 9;367(1–2):79–85.

51. Feng AL, Boraey MA, Gwin MA, Finlay PR, Kuehl PJ, Vehring R. Mechanistic models facilitate efficient development of leucine containing microparticles for pulmonary drug delivery. Int J Pharm. 2011;409(1):156–63.

52. Ógáin ON, Li J, Tajber L, Corrigan OI, Healy AM. Particle engineering of materials for oral

inhalation by dry powder inhalers. I—Particles of sugar excipients (trehalose and raffinose) for protein delivery. Int J Pharm. 2011 Feb 28;405(1–2):23–35.

53. Mishra J, Rades T, Löbmann K, Grohganz H. Influence of Solvent Composition on the Performance of Spray-Dried Co-Amorphous Formulations. Pharmaceutics. 2018;10(2):47.

Legend to Figures:

Figure 1 The experimental instruments, (a) CK-EDB, (b) Droplet chain setup.

Figure 2 Evaporation histories of water and ethanol microdroplets at different temperatures and 0% RH. Symbols: Experimental CK-EDB data, solid lines: Stefan-Fuchs model, dashed lines: Maxwell model.

Figure 3 Evaporation histories of 0.3:0.7 w/w water/ethanol mixtures at three different temperatures. Symbols: Experimental CK-EDB data, solid lines: Stefan-Fuchs model, dashed lines: Maxwell model.

Figure 4 (a) Evaporation histories of three different compositions of water and ethanol at 20 °C, (b) their predicted water mass fraction histories.

Figure 5 Evaporation histories of some water and ethanol mixtures using both the Stefan-Fuchs and Maxwell models compared to another numerical work at 200 °C (14).

Figure 6 The composition variation of a water/ethanol droplet with different initial water mass fractions in dry air at 20 °C, used to find the iso-compositional point.

Figure 7 The iso-compositional water mass fractions of water/ethanol mixtures and the corresponding droplet temperatures at different drying temperatures in dry air.

Figure 8 The evaporation rates, κ, of water/ethanol mixtures at the iso-compositional point compared to